



HAL
open science

Optimal Forcing Patterns for Coupled Models of ENSO

Andrew M. Moore, Javier Zavala-Garay, Youmin Tang, Richard Kleeman,
Anthony T. Weaver, Jérôme Vialard, Kamran Sahami, David L. T. Anderson,
Michael Fisher

► **To cite this version:**

Andrew M. Moore, Javier Zavala-Garay, Youmin Tang, Richard Kleeman, Anthony T. Weaver, et al..
Optimal Forcing Patterns for Coupled Models of ENSO. *Journal of Climate*, 2006, 19 (18), pp.4683-
4699. 10.1175/JCLI3870.1 . hal-00155074

HAL Id: hal-00155074

<https://hal.science/hal-00155074>

Submitted on 9 Jun 2021

HAL is a multi-disciplinary open access archive for the deposit and dissemination of scientific research documents, whether they are published or not. The documents may come from teaching and research institutions in France or abroad, or from public or private research centers.

L'archive ouverte pluridisciplinaire **HAL**, est destinée au dépôt et à la diffusion de documents scientifiques de niveau recherche, publiés ou non, émanant des établissements d'enseignement et de recherche français ou étrangers, des laboratoires publics ou privés.

Optimal Forcing Patterns for Coupled Models of ENSO

ANDREW M. MOORE,* JAVIER ZAVALA-GARAY,⁺ YOUMIN TANG,[#] RICHARD KLEEMAN,[@]
ANTHONY T. WEAVER,[&] JÉRÔME VIALARD,** KAMRAN SAHAMI,⁺⁺ DAVID L. T. ANDERSON,^{##} AND
MICHAEL FISHER^{##}

*Program in Atmospheric and Oceanic Sciences, and Cooperative Institute for Research in Environmental Sciences, University of Colorado, Boulder, Colorado

⁺Rosenstiel School of Marine and Atmospheric Science, University of Miami, Miami, Florida

[#]Environmental Science and Engineering, University of Northern British Columbia, Prince George, British Columbia, Canada

[@]Courant Institute of Mathematical Sciences, New York University, New York, New York

[&]Centre Européen de Recherche et de Formation Avancée en Calcul Scientifique/SUC URA 1875, Toulouse, France

**LODYC, Unité Mixte de Recherche CNRS, Université Paris, Paris, France

⁺⁺Department of Physics, Metropolitan State College of Denver, Denver, Colorado

^{##}European Centre for Medium-Range Weather Forecasts, Shinfield Park, Reading, Berkshire, United Kingdom

(Manuscript received 20 October 2004, in final form 30 December 2005)

ABSTRACT

The optimal forcing patterns for El Niño–Southern Oscillation (ENSO) are examined for a hierarchy of hybrid coupled models using generalized stability theory. Specifically two cases are considered: one where the forcing is stochastic in time, and one where the forcing is time independent. The optimal forcing patterns in these two cases are described by the *stochastic optimals* and *forcing singular vectors*, respectively. The spectrum of stochastic optimals for each model was found to be dominated by a single pattern. In addition, the dominant stochastic optimal structure is remarkably similar to the forcing singular vector, and to the dominant singular vectors computed in a previous related study using a subset of the same models. This suggests that irrespective of whether the forcing is in the form of an impulse, is time invariant, or is stochastic in nature, the optimal excitation for the eigenmode that describes ENSO in each model is the same. The optimal forcing pattern, however, does vary from model to model, and depends on air–sea interaction processes.

Estimates of the stochastic component of forcing were obtained from atmospheric analyses and the projection of the dominant optimal forcing pattern from each model onto this component of the forcing was computed. It was found that each of the optimal forcing patterns identified may be present in nature and all are equally likely. The existence of a dominant optimal forcing pattern is explored in terms of the effective dimension of the coupled system using the method of balanced truncation, and was found to be $O(1)$ for the models used here. The implications of this important result for ENSO prediction and predictability are discussed.

1. Introduction

On seasonal-to-interannual time scales, climate variability in the tropical Pacific is dominated by the El Niño–Southern Oscillation (ENSO). However, there is also significant large-scale synoptic atmospheric variability associated with equatorially trapped waves, organized mesoscale convective systems, and intrasea-

sonal variability [e.g., the Madden–Julian oscillation (MJO)]. On ENSO time scales this variability can be viewed as a stochastic process, and a growing body of literature suggests that a significant fraction of ENSO variability may be stochastically forced (e.g., Lau 1985; Lau and Chan 1985, 1986, 1988; Penland and Sardeshmukh 1995; Penland 1996; Blanke et al. 1997; Eckert and Latif 1997; Moore and Kleeman 1999ab; McPhaden 1999; Roulston and Neelin 2000; Zavala-Garay et al. 2003; Federov et al. 2003), an idea recently challenged by Chen et al. (2004) and discussed further by Anderson (2004).

The nature of the stochastic forcing is somewhat of an unresolved issue. Most studies of stochastic influ-

Corresponding author address: Andrew M. Moore, Program in Atmospheric and Oceanic Sciences, and Cooperative Institute for Research in Environmental Sciences, University of Colorado, Campus Box 311, Boulder, CO 80309-0311.
E-mail: amm@atoc.colorado.edu

ences on ENSO assume that the forcing is independent of the ENSO cycle, so-called additive forcing. However, it is known (e.g., Keen 1987; Kessler 2001) that MJO and westerly wind bursts are modulated significantly by the ENSO cycle, in which case the stochastic forcing will be a function of the underlying circulation, so-called multiplicative forcing. Multiplicative forcing can significantly alter the structure of the system probability density function (PDF) (Horsthemke and Lefever 1984), and some recent studies suggest that multiplicative effects may significantly influence ENSO variability (e.g., Lengaigne et al. 2004; Perez et al. 2005; Eisenman et al. 2005). Furthermore, there is a continuing debate on the relative role played by stochastic forcing versus nonlinear dynamics (e.g., Tziperman et al. 1994, 1995; An and Jin 2004), a debate largely fueled by small but significant departures of the observed ENSO PDF from a Gaussian distribution, a feature that linear dynamics fails to explain. Doubtless both stochastic and nonlinear influences are important, but here our focus is on stochastic influences.

There has been considerable recent progress in understanding the response of dynamical systems to stochastic forcing. If favorably aligned, stochastically induced perturbations can grow by extracting energy (or more generally variance) from the underlying flow. The resulting stochastically induced variance is a balance between variance input by the stochastic forcing, variance lost by dissipation, and variance liberated by perturbations from the underlying flow.

The seminal works of Farrell and Ioannou (1993, 1996a,b) on Generalized Stability Theory (GST) show that the release of variance from the stochastically forced underlying flow can be understood in terms of the linear superposition of the eigenmodes of the system. During the early stages of development, the evolution of stochastically induced perturbations is described by linear dynamics. Inhomogeneities in the underlying flow field render nonorthogonal the eigenmodes of the linear operators that describe perturbation development, meaning that they can linearly interfere. The resulting interference patterns can lead to rapid transient growth of perturbation amplitude, and maintain high variance.

GST provides a powerful framework for exploring the dynamics of perturbation growth and variance maintained by various kinds of forcing. Orthogonal bases can be identified that account for different fractions of perturbation growth due to impulsive forcing (singular vectors), forcing that is time invariant (forcing singular vectors), and forcing that is stochastic in nature (stochastic optimals). GST has been applied to ENSO by a number of investigators (e.g., Blumenthal 1991;

Penland and Sardeshmukh 1995; Penland 1996; Kleeman and Moore 1997; Moore and Kleeman 1996, 1997a,b, 1999a,b, 2001; Moore et al. 2003; Xue et al. 1994, 1997a,b; Thompson 1998; Johnson 1999; Fan et al. 2000; Zavala-Garay et al. 2003; Kleeman et al. 2003) in an attempt to understand its dynamics and limits of predictability. Most previous work has been limited to statistical models of ENSO or dynamical models of intermediate complexity. The effective dimension of these models appears to be quite small (Moore and Kleeman 2001), and as such the generality of the conclusions drawn from these studies, particularly in relation to the suggested link between ENSO and intraseasonal variability has been openly questioned. The purpose of the present study is to apply GST to more sophisticated coupled models of ENSO using general circulation model (GCM) components that potentially may possess many more degrees of freedom. We will show that many of the findings and conclusions from intermediate coupled models appear to be robust.

The coupled models used in the present study are described in section 2. GST—as it relates to optimal forcing patterns, the so-called stochastic optimals—is briefly reviewed in section 3, and applied to each coupled model. In section 4 we discuss a related set of optimal forcing patterns called forcing singular vectors, and note their similarity to the stochastic optimals. In sections 3 and 4 robust patterns of forcing are identified, and in section 5 we search for analogues of these patterns in estimates of stochastic forcing derived from atmospheric analyses. The effective dimension of the system is explored using the method of balanced truncation in section 6, and we conclude with a summary and conclusions in section 7.

2. The coupled models

Three hybrid coupled models of ENSO were used, and each shares the same Ocean GCM (OGCM) coupled to three different atmospheric models. The choice of models was motivated by that fact that: (i) atmospheric model physics significantly impacts perturbation growth (Moore and Kleeman 2001; Moore et al. 2003), and (ii) the models were readily available. Each atmospheric model emphasizes different aspects of air–sea interaction in the Tropics, and it is the impact of these processes on the coupled system that we explore here.

a. The ocean model

The primitive equation OGCM common to each coupled model is Océan Parallélisé (OPA) 8.1 (Madec

et al. 1998) configured for the tropical Pacific Ocean (30°N–30°S, 120°E–75°W) (Vialard and Delecluse 1998a,b; Vialard et al. 2001), with 1° resolution, increasing in the meridional direction from 0.5° between 5°N and 5°S to 2° at 30°N and 30°S. There are 25 levels in the vertical with 10-m thickness in the upper 150 m, and realistic bathymetry and coastal geometry are included.

Prior to coupling with each atmospheric model, the OGCM was first spun up for 30 yr using (i) climatological monthly mean winds derived either from the Florida State University (FSU; Legler and O'Brien 1985; Stricherz et al. 1992) or the National Centers for Environmental Prediction–National Center for Atmospheric Research (NCEP–NCAR; Kalnay et al. 1996) reanalysis wind products; (ii) a surface heat flux $Q = Q_h + \varepsilon(T - T_r)$ where Q_h is the 15-yr European Centre for Medium-Range Weather Forecasts (ECMWF) Re-Analysis (ERA-15) climatological seasonal cycle, T is model SST, T_r is the climatological mean observed seasonal cycle of SST from Reynolds and Smith (1994), and $\varepsilon = -40 \text{ W m}^{-2} \text{ K}^{-1}$; (iii) the annual mean net freshwater flux forcing Q_s composed of ERA-15 net ($E - P$) and a relaxation to the annual mean sea surface salinity of Levitus (1982). At the end of each spinup there are no significant long-term trends in the upper-ocean circulation. Next the OGCM was run using the actual monthly mean FSU or NCEP–NCAR reanalysis winds for the period 1960–99 with Q and Q_s as above.

b. Coupled models 1F and 1N

“Model 1F” and “model 1N” consist of the OGCM coupled to statistical models of the atmosphere constructed using singular value decomposition (SVD) analysis and principal component analysis (PCA) of monthly mean SST anomalies (SSTAs) of the OGCM (from the last 30 yr of the OGCM spinup, 1970–99) and the monthly mean wind stress anomalies (WSAs) (FSU for model 1F, NCEP–NCAR for model 1N). Similar models have been used by others (e.g., Latif and Villwock 1990; Latif and Flügel 1991; Balmaseda et al. 1995; Syu et al. 1995; Kleeman et al. 1999). In model 1F, SVD analysis was performed on the covariance matrix of SSTAs and WSAs computed from the entire 30-yr period. In the case of model 1N, seasonal variations of covariance between SSTA and WSA were accounted for by performing PCA for each calendar month (i.e., for each month there is essentially a different atmospheric model) and a linear regression between the leading principal components computed following Barnett et al. (1993; see Tang et al. 2004a for details).

In model 1F (1N) the OGCM was forced by the sum

of the FSU (NCEP) monthly mean climatological winds and the wind anomalies computed from the statistical atmospheric model in response to OGCM SSTAs relative to the spinup.

c. Coupled model 2

“Model 2” consists of the OGCM coupled to the Kleeman (1991) global, two-level, steady-state, anomaly atmospheric model, a good approximation in the Tropics (Webster 1972; Gill 1980). The atmosphere is heated by Newtonian relaxation to SSTA, and by latent heating due to deep convection via a simple moist static energy–dependent convection scheme. SSTAs were computed as in models 1F and 1N and passed to the atmospheric model. The OGCM was forced by the sum of the wind anomalies and the FSU monthly mean climatological winds.

3. Stochastic optimal of the coupled models

Synoptic-to-intraseasonal variability can be viewed as a stochastic forcing that induces perturbations in the system. We denote by \mathbf{s} the perturbation state vector of each coupled model, and assume that to first order, the evolution of \mathbf{s} is described by

$$d\mathbf{s}/dt = \mathbf{A}\mathbf{s} + \mathbf{f}(t), \quad (1)$$

where \mathbf{A} represents the tangent-linear operator of either model 1F, 1N, or 2 linearized about a circulation of interest, denoted \mathbf{S}_0 , and $\mathbf{f}(t)$ represents the stochastic forcing.

The stochastically induced variance will depend on the properties of the linear operator \mathbf{A} . For red noise the maximum response occurs when $\mathbf{f}(t)$ takes the form of the leading eigenvectors of $\mathbf{Q}(t_1, t_2) = \int_{t_1}^{t_2} \int_{t_1}^{t_2} e^{-|t''-t'|/t_c} \mathbf{R}^T(t_2, t'') \mathbf{X} \mathbf{R}(t', t_2) dt' dt''$, where $\mathbf{R}(t_1, t_2)$ denotes the propagator of the unforced form of (1), \mathbf{X} is a real symmetric positive-definite matrix defining the variance norm, and t_c is the decorrelation time of $\mathbf{f}(t)$. Eigenvectors \mathbf{q}_i of \mathbf{Q} with associated eigenvalue q_i are called the stochastic optimal (SOs; see Farrell and Ioannou 1993, 1996a,b and Kleeman and Moore 1997 for more details).

The propagator \mathbf{R} and its transpose (the adjoint propagator) are $(7 \times 10^5) \times (7 \times 10^5)$ matrices and are never explicitly evaluated. Instead the action of \mathbf{R} and \mathbf{R}^T on \mathbf{s} can be computed by respectively integrating the tangent-linear and adjoint versions of models 1F, 1N, and 2. The operation described by \mathbf{Q} can be affected by forcing the adjoint coupled model (described by \mathbf{R}^T) with a time-weighted integral of the tangent-linear coupled model dynamics given by $\int_{t_1}^{t_2} e^{-|t''-t'|/t_c} \mathbf{X} \mathbf{R}(t', t_2) dt'$ once t_c and \mathbf{X} have been identified. The eigenvectors of \mathbf{Q} were evaluated iteratively

using ARPACK (Lehoucq et al. 1998). The tangent-linear and adjoint versions of the OGCM and the Kleeman (1991) atmospheric model were developed directly from the nonlinear FORTRAN code using the recipe of Giering and Kaminski (1998) as described in Weaver et al. (2003) and Moore and Kleeman (1996), respectively. The adjoint statistical atmospheres of models 1N and 1F are trivial to compute.

A useful measure of the low-frequency ENSO variability is the square of the Niño-3 index, the measure of stochastically induced variance used here. It is possible to compute SOs for either two- or three-dimensional stochastic forcing, the former being where the stochastic forcing is surface momentum (τ), heat (H), and $(E - P)$ freshwater fluxes, while for the latter the stochastic forcing is for each prognostic variable at every model grid point. Here we consider 2D SOs because of their relevance to ENSO.

The ideas described here can be applied to stable and unstable systems. Stability was controlled using a scaling parameter α to adjust the amplitude of wind anomalies imposed on the OGCM. By varying α it was possible to control the sign of the real part of the largest eigenvalue, λ_0 , of \mathbf{A} . For $\text{Re}(\lambda_0) \sim 0$, the model resides near the primary bifurcation point, the case considered here; λ_0 versus α for models 1F and 2 is presented in Moore et al. (2003), and a similar analysis was performed for model 1N (not shown).

The eigenvector equation $\mathbf{Q}\mathbf{q}_i = q_i\mathbf{q}_i$ can also be expressed as $q_i = \mathbf{q}_i^T \mathbf{Q} \mathbf{q}_i / \mathbf{q}_i^T \mathbf{q}_i$, raising the issue of the physical meaning of $\mathbf{q}_i^T \mathbf{q}_i$ when the elements of \mathbf{q}_i have different physical dimensions, since it is customary to normalize the SOs so that $\mathbf{q}_i^T \mathbf{q}_i = 1$. To circumvent this issue we first considered each component of the stochastic forcing independently [i.e., τ alone, H alone, $(E - P)$ alone], so that in each case $\mathbf{q}_i^T \mathbf{q}_i$ has the same physical dimensions throughout. Experiments revealed, however, that combining the three separate SO calculations into a single calculation where \mathbf{q} is composed of τ , H , and $(E - P)$ yields essentially identical SO patterns for each component of \mathbf{q} when compared to those computed separately, despite the disparity in physical dimensions in the former case. Thus each SO component can be treated in isolation with independent amplitude.¹

a. Annual mean basic state

We consider first the SOs when \mathbf{S}_0 describes annual mean conditions. In this case \mathbf{S}_0 was the annual mean

¹ Calculations using a nondimensionalized \mathbf{q} (not shown) also yield identical patterns to those shown later.

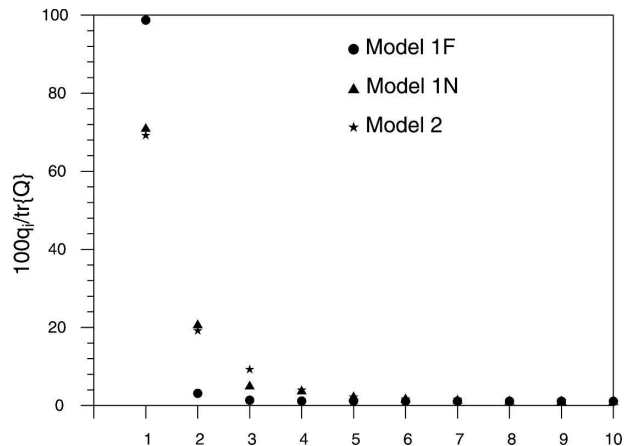


FIG. 1. A plot of $100q_i/\text{tr}[\mathbf{Q}]$ for the first 10 members ($i = 1, \dots, 10$) of the SO spectrum for each coupled model and an annual mean basic state. If the stochastic forcing projects equally onto each SO then $100q_i/\text{tr}[\mathbf{Q}]$ represents the fraction of stochastically induced variance explained by each SO.

basic state of each model component run separately subject to observed boundary conditions. Choosing \mathbf{S}_0 to be time invariant renders (1) autonomous, in which case the eigenvectors of \mathbf{A} form a unique basis for studying the dynamics of the circulation. While \mathbf{S}_0 is not a model solution, analysis of the associated autonomous system is an important first step because of the unique nature of the system eigenmodes. The time mean circulation is likely to be more stable than any instantaneous flow field (Pedlosky 1987, chapter 7) placing a lower bound on the response to stochastic forcing. A similar approach has been used extensively in meteorology for many years (e.g., Simmons and Hoskins 1976; Frederiksen 1982; and references therein; Simmons et al. 1983; Borges and Hartmann 1992; Molteni and Palmer 1993). Time-dependent (i.e., nonautonomous) operators will be explored in sections 3b and 3c.

1) BASIC SO PROPERTIES

First, consider the case where the stochastic forcing is assumed to be white in time, and $t_2 - t_1 = 365$ days for $\mathbf{Q}(t_1, t_2)$. The sensitivity of the SOs to these choices will be discussed in section 3a(2). If $\mathbf{f}(t)$ projects equally onto each SO then \mathbf{q}_i accounts for $100q_i/\text{tr}[\mathbf{Q}(t_1, t_2)]$ percent of the stochastically induced variance at time t_2 , and $100q_i/\text{tr}[\mathbf{Q}(t_1, t_2)]$ is a convenient way of viewing the SO spectrum, and is of theoretical interest. Figure 1 shows a plot of $100q_i/\text{tr}[\mathbf{Q}(t_1, t_2)]$ for the first 10 members of the SO spectrum for each model, and in each case the SO spectrum is dominated by \mathbf{q}_1 . We will demonstrate in section 5 that in fact \mathbf{q}_1 may account for almost 25% of the variance of $\mathbf{f}(t)$ computed from at-

mospheric analyses. The spectra in Fig. 1 for models 1F and 2 are qualitatively very similar to those shown in Moore et al. (2003) for the singular vectors (SVs) of the same models.² Model 1N was not used in Moore et al. (2003) but we anticipate that the same result would hold.

Since the SO spectra are dominated by one member, we show only \mathbf{q}_1 for each model. Figures 2, 3, and 4 show the (τ_x, τ_y) , (H) , and $(E - P)$ components of \mathbf{q}_1 for each model computed using the annual mean basic state: \mathbf{q}_1 is typically large scale, except for τ_y . Since each component of \mathbf{q}_1 can be considered as independent, as discussed above, the relative forcing amplitudes of each component are arbitrary. Note also that $(\tau_x, \tau_y, H, E - P)$ for \mathbf{q}_1 is very similar to the surface structure of (u, v, T, S) of the dominant SV of each coupled model at initial time for the same time period using a norm based on ocean temperature alone (Moore et al. 2003).

Experiments in which each model is subject to stochastic forcing composed of each SO with realistic amplitude (Tang et al. 2005) reveal that the $(E - P)$ and τ_y components contribute very little to the stochastically induced variance in each model, so we will neglect $(E - P)$ and τ_y . The SOs of Figs. 2, 3, and 4 are generally confined to the equatorial waveguide, although for models 1N and 2, some off-equatorial regions are favored by H such as the warm regions of the SW Pacific and coastal Central America where deep convection anomalies are possible in model 2. For model 1F, τ_x favors the central and east Pacific, while in models 1N and 2 it is the central and west Pacific that are favored. In models 1F and 1N, H forms a dipole spanning the entire Pacific, while in model 2 it is the west Pacific that is preferred.

The similarity in structure between the dominant SV at initial time and the SO patterns and their corresponding spectra is consistent with the fact that each model appears to possess a single dominant low-frequency coupled ocean-atmosphere mode that describes ENSO (Moore et al. 2003). This suggests that regardless of how the models are perturbed (i.e., an impulse versus continuous stochastic forcing) there appears to be a unique optimal spatial structure for the forcing. We return to this point in sections 4 and 6.

2) SENSITIVITY STUDIES

The SOs of the annual mean basic state were also computed by varying $(t_2 - t_1)$ between 3 and 24 months,

² Singular vectors are the fastest growing of all possible perturbations in the linear limit and maximize growth of the chosen norm. Using the above notation they are the eigenvectors of $\mathbf{R}^T(t_2, t_1)\mathbf{X}\mathbf{R}(t_1, t_2)$.

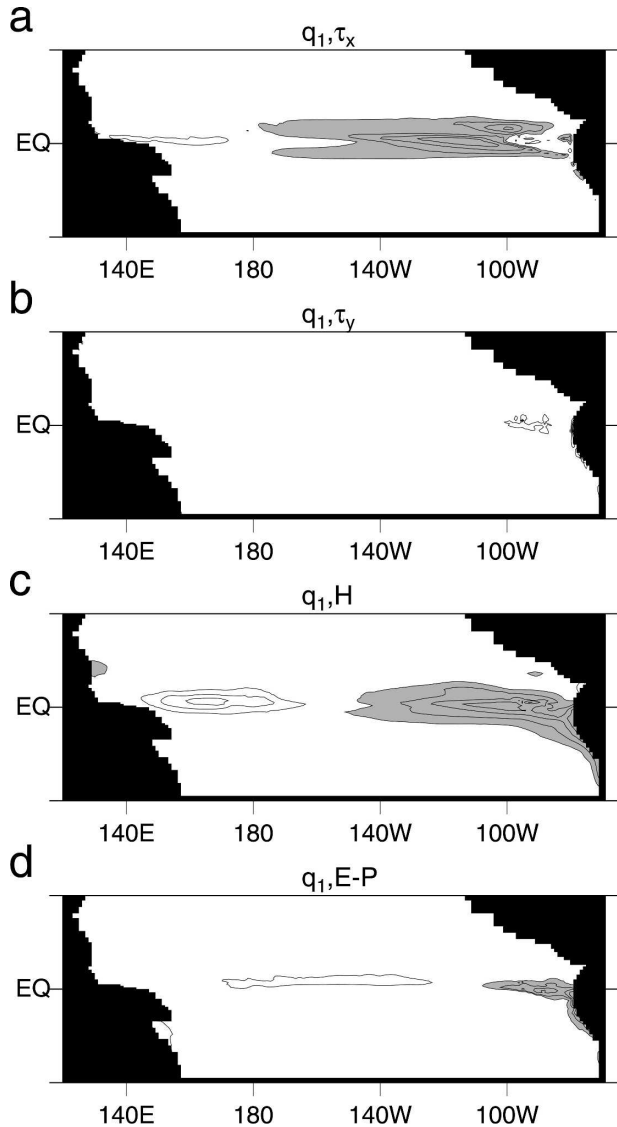


FIG. 2. The spatial structure of wind stress (τ_x, τ_y) , surface heat flux H and surface freshwater flux $(E - P)$ for \mathbf{q}_1 for model 1F and an annual mean basic state. In each case the contour interval is arbitrary, and shaded and unshaded regions are of opposite sign.

and the structure of \mathbf{q}_1 was found to vary little. In general, \mathbf{q}_1 for models 1F and 2 is less pronounced in the west Pacific for $t_2 - t_1 = 3$ months compared to longer intervals, consistent with the role of equatorial Kelvin waves on the ENSO dynamics of these models. For short $t_2 - t_1$ there is insufficient time for Kelvin waves to cross the basin and influence the tropical eastern Pacific, so a more effective way of exciting variability in the Niño-3 region is to directly perturb the east.

The SOs are also insensitive to the temporal decorrelation time of the stochastic forcing, t_σ which was varied between one model time step (i.e., white noise)

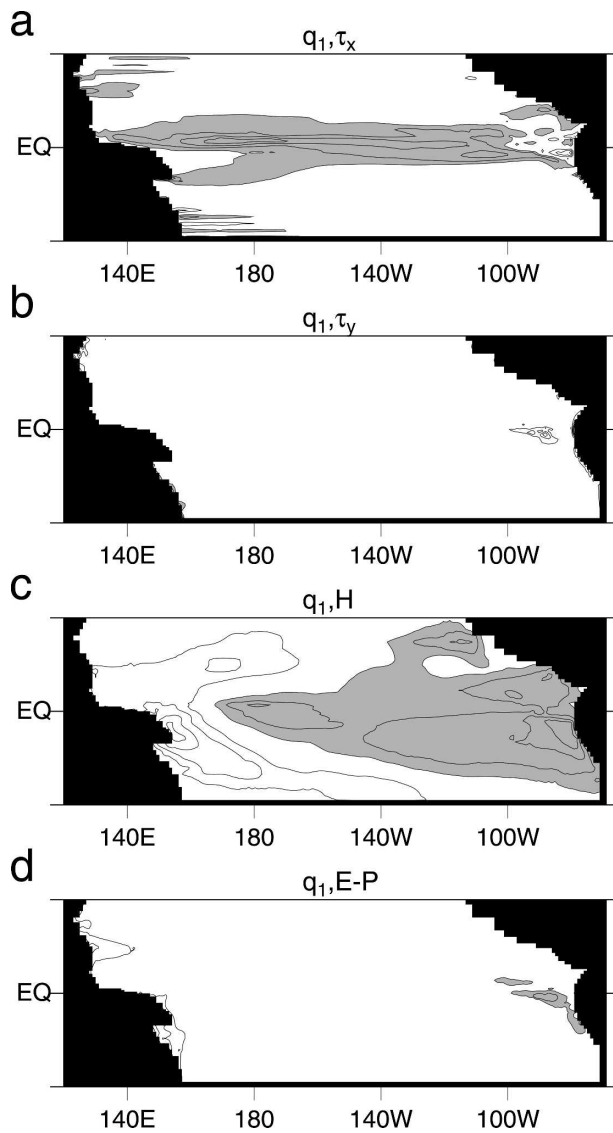


FIG. 3. Same as Fig. 2 except for model 1N.

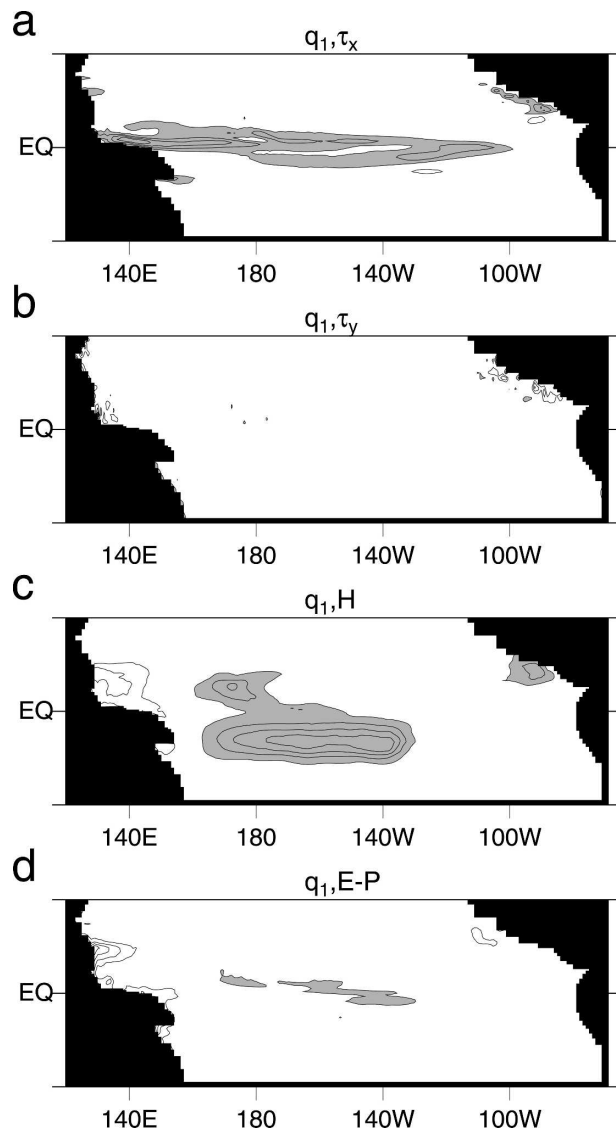


FIG. 4. Same as Fig. 2 except for model 2.

and 9 months. We also explored the sensitivity of the SOs to the choice of norm associated with \mathbf{X} . The leading SO is essentially unchanged if we use the squared Niño-3 index, Niño-4 index, or Niño-1 + Niño-2 indexes. For norms that are good indicators of ENSO variability (i.e., norms based on the upper-ocean thermal structure) the structure of \mathbf{q}_1 is relatively insensitive to the choice of norm, a result that mirrors that of the SVs described in Moore et al. (2003). In addition, the patterns of $(\tau_x, \tau_y, H, E - P)$ for the 2D SOs and those of the surface components of (u, v, T, S) for the 3D SOs are very similar.

The coupled models were all tuned to be close to the primary bifurcation point (i.e., the point where they can support self-sustaining oscillations) since this is one of

the more interesting and perhaps most relevant dynamical regimes for ENSO. In this case \mathbf{q}_1 is relatively insensitive to whether the system is just above or just below the bifurcation point. When the system is far below the bifurcation point, the structure of \mathbf{q}_1 differs somewhat from that considered here (not shown). As α decreases and the ENSO mode becomes more stable the shape of the spectra in Fig. 1 remain largely unchanged, although the relative separation of the first two eigenvalues decreases, but even for small α the first SO dominates (not shown).

b. The seasonal cycle

Next we explore how the SOs are influenced by a nonautonomous \mathbf{A} , and specifically by the phase of the

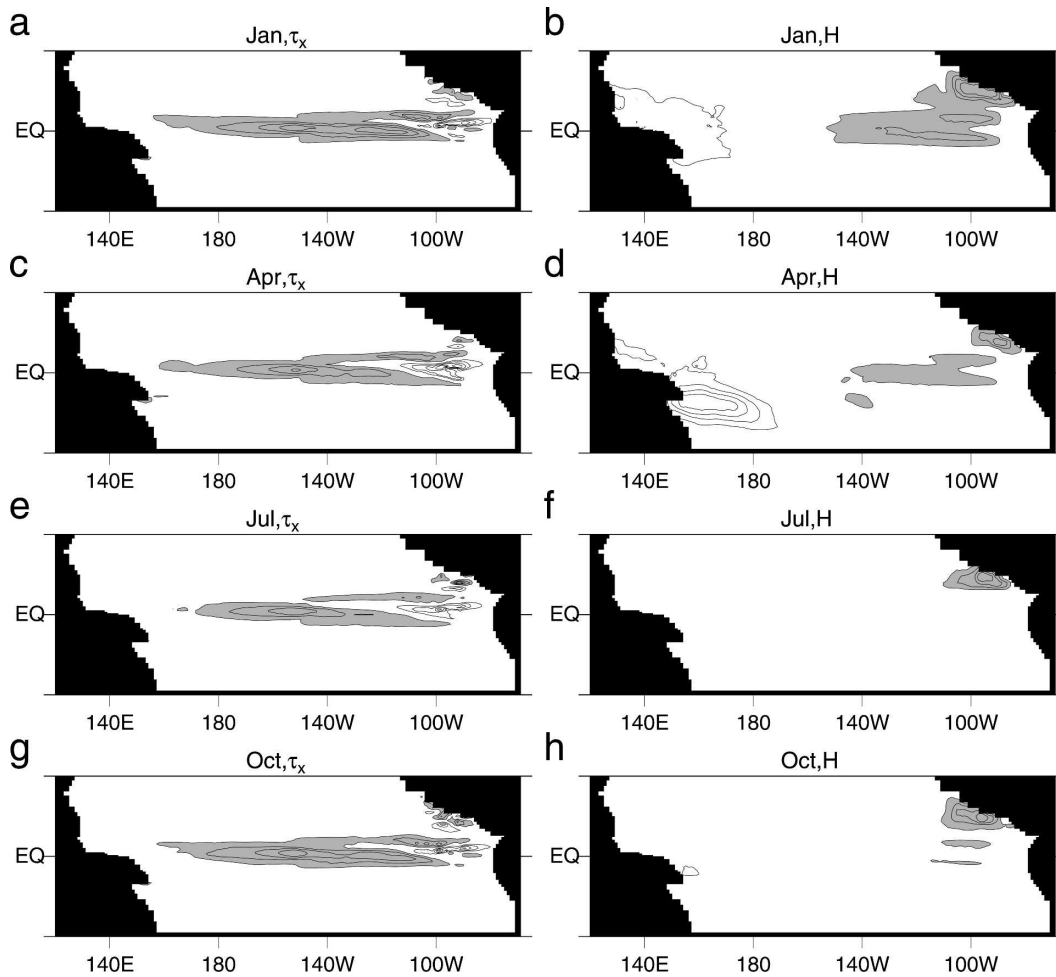


FIG. 5. The spatial structure of τ_x and H for \mathbf{q}_1 computed from model 2 and a seasonally varying basic state with start date (a), (b) 1 Jan; (c), (d) 1 Apr; (e), (f) 1 Jul; and (g), (h) 1 Oct. In each case the contour interval is arbitrary, and shaded and unshaded regions are of opposite sign.

seasonal cycle. In this case \mathbf{S}_0 is the monthly average seasonal cycle of each component of the coupled system run separately and interpolated linearly in time. Four sets of SOs were computed for each model by computing $\mathbf{Q}(t_1, t_2)$ for $t_2 - t_1 = 365$ days, where $t_1 = 0$ corresponds to 1 January, 1 April, 1 July, and 1 October, and $\mathbf{f}(t)$ white in time. The rationale was to explore whether the relative phase of the seasonal cycle during the 365-day period has any significant effect on the SOs compared to the case of annual mean \mathbf{S}_0 . The case $t_2 - t_1 = 180$ yields qualitatively similar results (not shown).

For models 1F and 1N, the SO patterns (not shown) were all very similar to those for annual mean \mathbf{S}_0 (cf. Figs. 2 and 3), irrespective of start date. In contrast, the phase of the seasonal cycle does influence the SOs of model 2 as shown in Fig. 5, where the H structure of \mathbf{q}_1 varies considerably. For all start dates, the model 2 SOs

have an H component that favors coastal Central America, while the west Pacific is favored only for the 1 April start. For a 1 January start date, H is mainly in the tropical east Pacific, with some signature in the west. For the 1 April start date, H is confined mainly to the tropical west Pacific; H for a 1 July start date exhibits no signature in the equatorial east or west Pacific, but for a 1 October start some of the equatorial signature begins to reappear. Further experiments (not shown) reveal that the seasonal shifts in H are due to seasonal variations in the basic state atmospheric heating. Interestingly the average of the H patterns in Fig. 5 does not resemble H for \mathbf{q}_1 of the annual mean \mathbf{S}_0 in Fig. 4c.

The \mathbf{q}_1 structure of τ_x for model 2 appears relatively insensitive to the time of year and is controlled by ocean dynamics for the chosen norm, as demonstrated by computing the SOs for the OGCM alone using the

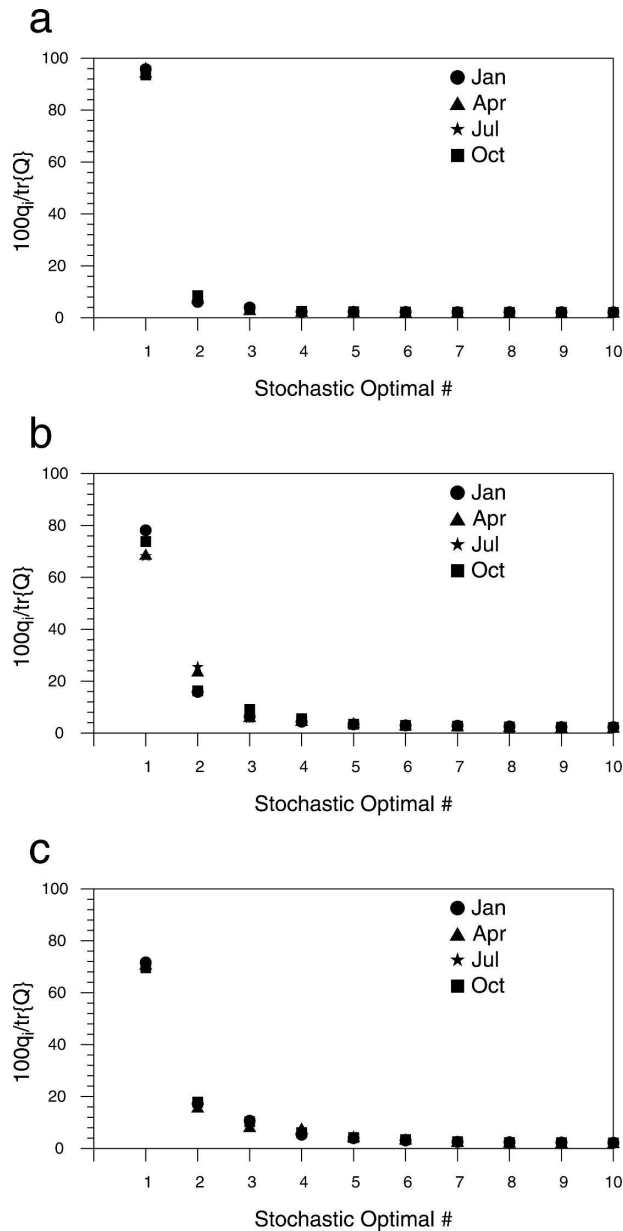


FIG. 6. Plots of $100q_i/\text{tr}[\mathbf{Q}]$ for the first 10 members ($i = 1, \dots, 10$) of the SO spectrum as a function of start date using a seasonally varying basic state: (a) model 1F, (b) model 1N, and (c) model 2.

squared Niño-3 index norm. This is not, however, a general result since other temperature-based norms yield very localized SOs associated with local shear and frontal regions, reminiscent of the OGCM SVs described by Moore et al. (2003).

Figure 6 shows $100q_i/\text{tr}[\mathbf{Q}(t_1, t_2)]$, $i = 1, \dots, 10$ for each model as a function of start date. In each case \mathbf{q}_1 dominates the spectrum, there is little seasonal variation in the explained variance, and $100q_i/\text{tr}[\mathbf{Q}(t_1, t_2)]$ is very similar to the annual mean case (Fig. 1).

c. The ENSO cycle

The sensitivity of the SOs to the phase of the ENSO cycle was explored using actual hindcasts made with each model for 1980–99. The resulting SOs for models 1N and 2 have also been used to generate hindcast ensembles to explore ENSO predictability (Tang et al. 2004b, 2005). The coupled models were initialized using the ocean data assimilation method described by Tang et al. (2003), and 12-month hindcasts were run with start dates 1 January, 1 April, 1 July, and 1 October each year. Only models 1N and 2 were considered in this case because of the inferior hindcast skill of model 1F. In the case of model 1N, α was reduced by 40% to match that used by Tang et al. (2003). For lead times less than 6 months, model 1N hindcast skill for Niño-3 SST anomalies (rms error and anomaly correlation) was found to be relatively insensitive to α , although \mathbf{q}_1 does change somewhat [see section 3a(b)].

An issue here is the validity of the tangent-linear assumption. Using the same OGCM, Weaver et al. (2003) showed that for the large scales of motion typically associated with ENSO, the tangent-linear assumption is valid for periods ~ 6 months. However, in addition to the large-scale seasonal-to-interannual time-scale phenomena, the OGCM also resolves tropical instability waves (TIWs; Vialard et al. 2003). The tangent-linear assumption associated with TIWs is violated on the time scale of a month or less (Weaver et al. 2003) presumably because of the existence of rapidly growing unstable eigenmodes of \mathbf{A} associated with the shear between the equatorial currents of the eastern and central equatorial Pacific. Interestingly such modes do not appear when \mathbf{S}_0 is defined by the annual mean or seasonal cycle.

A dual approach was adopted in an attempt to minimize the excitation of TIWs associated with \mathbf{S}_0 defined by hindcasts. First, as in sections 3a and 3b, the squared Niño-3 index was adopted as the variance norm since it is reasonable to assume that the spatial patterns of positive and negative SST anomalies associated with TIWs will, by and large, spatially average to zero over the Niño-3 region. Second, a linear interpolation of the monthly averaged hindcast model trajectory was used to define \mathbf{S}_0 because monthly averages are more stable than instantaneous flows. While this dual approach was successful most of the time, there were periods when some SOs consistently favored the TIW region for growth, presumably because of the propensity for even the monthly mean ocean circulation to support rapidly growing unstable modes that do not spatially average to zero in the Niño-3 region. The τ_x structure of a typical SO associated with TIW generation is shown in Fig. 7.

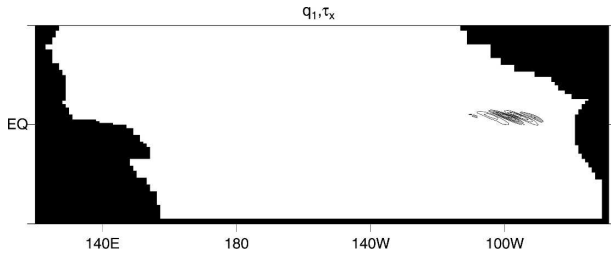


FIG. 7. A typical τ_x component of \mathbf{q}_1 when the TIW generation region is favored by the SOs of individual model hindcasts. The contour interval is arbitrary and shaded and unshaded regions are of opposite sign.

The optimal excitations of the TIWs are small scale and distinct from the large-scale SOs associated with ENSO.

As noted in section 3b, the SOs of the seasonal cycle identify geographic regions where stochastically induced perturbations associated with ENSO are likely to undergo rapid growth. In addition, these areas appear to be fairly robust, varying only with the phase of the seasonal cycle. The same areas of preferred perturbation growth were also found throughout the ENSO cycle of individual hindcasts. However, there are two important points to note: 1) the structure of the large-scale SOs of ENSO compared to those of the seasonal cycle is significantly influenced by the time evolution of \mathbf{S}_0 ; 2) the position of the large-scale SOs within the spectrum varies with \mathbf{S}_0 , as does the fraction of stochastically induced variance $100q_i/\text{tr}[\mathbf{Q}(t_1, t_2)]$ they describe. To explore how these properties vary from one hindcast to the next, we computed diagnostic quantities designed to isolate the optimal excitation for ENSO in each case. This approach is also useful for summarizing what is clearly a large number of SO patterns (i.e., 20 yr \times 4 start dates per year \times 10 SO patterns per start date).

The dominant SO of ENSO associated with each start date in section 3b (i.e., where \mathbf{S}_0 defines the seasonal cycle) was viewed as the representative SO of hindcasts started at the same time of the year. We will denote these SOs as $\mathbf{q}_{1,n}^r$ where $n = 1, \dots, 4$ and $n = 1$ corresponds to a 1 January start, $n = 2$ to a 1 April start, and so forth. The spatial correlation of the $\mathbf{q}_{1,n}^r$ with each of the first 10 members of the hindcast SO spectra, for the appropriate start date given by n , identifies the analog of $\mathbf{q}_{1,n}^r$ associated with each hindcast. The hindcast SOs with the maximum spatial correlation were identified, and the corresponding correlations for τ_x and H denoted ρ_τ and ρ_H , respectively. The fraction of stochastically induced variance associated with the SO with spatial correlations ρ_τ and ρ_H was also computed according to $100q_i/\text{tr}[\mathbf{Q}(t_1, t_2)]$ and will be denoted V_m .

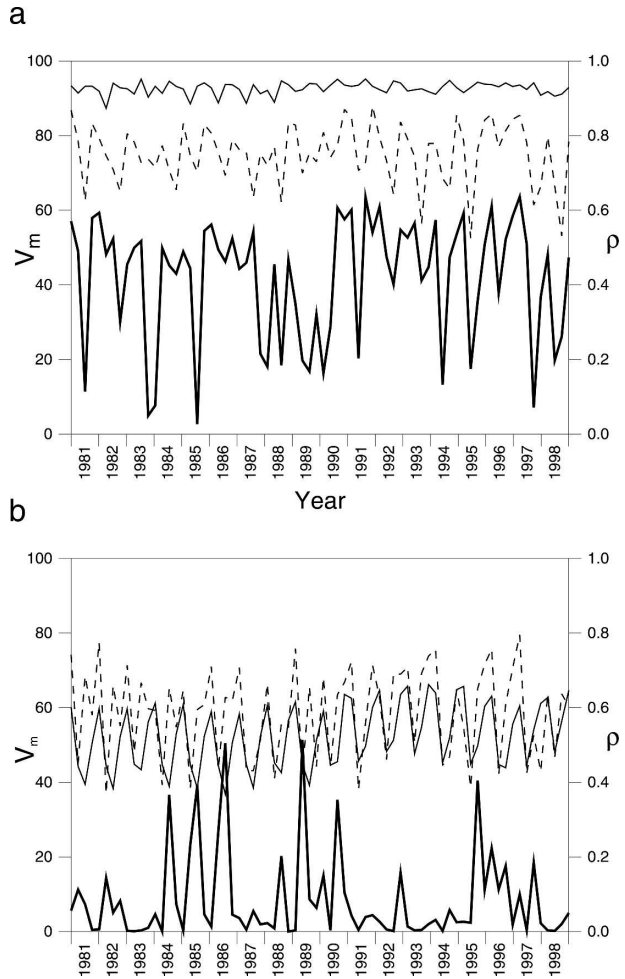


FIG. 8. The correlation diagnostic ρ_τ (solid line), ρ_H (dashed line), and variance diagnostic V_m (heavy solid line) vs start date using hindcast basic-state trajectories from (a) model 1N and (b) model 2. Each diagnostic is defined in section 3c such that ρ_τ and ρ_H are measures of the similarity of the SO \mathbf{q}_i for $i = 1, \dots, 10$, which most closely resembles the \mathbf{q}_1 of the corresponding phase of the seasonal cycle discussed in section 3b. Here V_m is the value of $100q_i/\text{tr}[\mathbf{Q}]$ for the SO identified by ρ_τ and ρ_H .

In all cases we chose $t_2 - t_1 = 365$ days and assumed white noise forcing in time.

Figure 8 shows ρ_τ , ρ_H , and V_m versus hindcast start date. In each case, particularly for model 1N (Fig. 8a), ρ_τ and ρ_H are relatively high, indicating that a large-scale SO pattern exists similar to that of the corresponding phase of the seasonal cycle of (i.e. $\mathbf{q}_{1,n}^r$). The spatial correlations are somewhat lower in model 2 (Fig. 8b) than in model 1N and exhibit a pronounced seasonal cycle due to the fact that during model 2 hindcasts the western Pacific and Central American coast are almost never favored by the H components of the SOs. The H patterns for the model 2 SOs are primarily located in the central and east Pacific, indicating that

anomalous convective heating in the atmosphere over the warm pool and coastal Central America is less active during hindcasts than during the climatological seasonal cycle. Further experiments (not shown) reveal that this is due primarily to the tendency of the ocean surface to systematically cool in the west during the course of a 12-month hindcast, placing the atmosphere below the moist static energy threshold for perturbation deep convection.

Here V_m is an excellent indicator of when the SOs associated with the TIWs (cf. Fig. 7) emerge. When this occurs, the large-scale coherent patterns $\mathbf{q}_{1,m}^f$ associated with the seasonal cycle are no longer dominant and occupy a position further down the spectrum and as such V_m decreases dramatically. Figure 8 shows that the two coupled models behave quite differently in this respect. In model 1N (Fig. 8a), aperiodic decreases in V_m occur for different start dates, but by and large the SO associated with ρ_r and ρ_H is often dominant (i.e., large V_m also). For model 2 (Fig. 8b) V_m is very small for many of the hindcasts, indicating that the TIW region is preferred for stochastically induced perturbation growth. Figure 8b also shows that V_m is typically largest in model 2 during hindcasts with a 1 July start date, indicating that the SO associated with ρ_r and ρ_H (cf. Figs. 5e,f) typically dominates for these cases. Low values of V_m do not mean that no large-scale SO is present, only that it does not occupy pole position in the spectrum; the relatively large values of ρ_r and ρ_H indicate that much of the time the large-scale SOs of Fig. 5 are present. The low values of V_m are most likely an indication that TIW activity is greater during model 2 hindcasts than during those of model 1N, although this has not been explored.

Generally, the SO spectrum is typically dominated by one SO member (not shown), although there are often times when this is not the case and the spectrum is rather flat. By and large, there is no discernible relationship between the shape of the SO spectrum and the phase of the seasonal cycle or ENSO cycle.

d. Nonnormality as a control of SO structure

The structure of the SOs depends on the model dynamics responsible for maintaining variance in the chosen norm. In the equation that describes the time evolution of the norm, there will be terms that describe (i) the generation of variance directly by the stochastic forcing, (ii) destruction of variance by dissipation, and (iii) source/sink terms due to the gain and loss of variance associated with \mathbf{S}_0 . If the source/sink terms are weak, or collocated with the region in which variance is measured, the most effective means of generating variance is by local forcing, and the SOs will favor the

region that defines the norm (i.e., in our case Niño-3). On the other hand, if the source/sink terms are large, and not collocated with the region defining the norm, remote or nonlocal forcing may be a more efficient means of generating variance, in which case the SOs may favor regions other than the region associated with the norm.

An alternative view of these same ideas is offered by GST in terms of the geometry of the system eigenmodes, where the sources of variance associated with \mathbf{S}_0 can be viewed in terms of a linear superposition of the nonorthogonal eigenmodes of the system. The resulting evolution of such perturbations is initially characterized by superexponential growth, which can far exceed that due to the most unstable eigenmode of the system, if indeed such a mode exists. The variance sustained by nonmodal growth depends on how nonnormal the system described by (1) happens to be, since it is the nonnormal character of \mathbf{A} that allows its nonorthogonal eigenmodes to linearly interfere. Nonmodal growth of the norm associated with this process can be identified with the source terms of variance associated with \mathbf{S}_0 in the norm evolution equation (e.g., Chhak et al. 2006), and here nonnormality is strongly controlled by the air-sea interaction processes (Moore and Kleeman 2001; Moore et al. 2003). In models 1F and 1N the number of coupled ocean-atmosphere modes is dictated by the number of SVD or EOF patterns retained, in the present case only two. This means that only two independent linear combinations of surface wind and SST anomalies are possible that define the quadrature phases of the ENSO mode (see also Roulston and Neelin 2003). Moore and Kleeman (2001) and Moore et al. (2003) also showed that such low-dimensional statistical atmospheric models yield operators \mathbf{A} in (1) that are more normal than coupled models that include the Kleeman (1991) dynamical atmosphere. The more normal a system happens to be, the more the SOs resemble the structure of the eigenmode that they tend to excite. The more nonnormal the system, then the more dissimilar the SOs are compared to this eigenmode.

In the case of models 1F and 1N, the small number of degrees of freedom of the statistical atmospheric component (i.e., two) renders these coupled models more normal than model 2, which has potentially many more degrees of freedom by virtue of its dynamical atmosphere. Thus the SOs of models 1F and 1N tend to resemble one phase of the ENSO mode in these models, and the most efficient way to stochastically induce variance is by inducing perturbations that resemble the ENSO mode, which also corresponds to locally forcing variance in the Niño-3 region.

For model 2, the SOs have a very different structure

to the ENSO mode because, in this case, atmospheric heating associated with deep penetrative convection increases the degree of nonnormality of the system (Moore and Kleeman 2001). In this case a more efficient means of generating variance is to perturb the system in the west Pacific, resulting in ENSO that manifests itself farther east as an increase in variance in the Niño-3 region. Physically, it is inhomogeneities in the atmospheric wind and specific humidity fields that render model 2 more nonnormal than its statistical counterpart.

4. Forcing singular vectors of the coupled models

Another problem of interest is the case where \mathbf{f} is time independent, and solutions of (1) can be written $\mathbf{s}(t_2) = \mathbf{R}(t_1, t_2)\mathbf{s}(t_1) + \mathbf{M}(t_1, t_2)\mathbf{f}$, where $\mathbf{M}(t_1, t_2) = \int_{t_1}^{t_2} \mathbf{R}(t, t_2)dt$. If $\mathbf{s}(t_1) = 0$, it is of interest to ask what form \mathbf{f} must take in order to maximize the response. The relevant time-invariant forcing \mathbf{f} is the eigenvector with the largest eigenvalue of $\mathbf{M}^T(t_2, t_1)\mathbf{X}\mathbf{M}(t_1, t_2)$. The eigenvectors of $\mathbf{M}^T(t_2, t_1)\mathbf{X}\mathbf{M}(t_1, t_2)$ are referred to as forcing singular vectors (FSVs; Barkmeijer et al. 2003).

In addition to the SOs of each basic state we have also computed the FSVs. Since the matrix \mathbf{X} that defines the squared Niño-3-index is rank 1, there is only one FSV for each basic state. Figure 9 shows the τ_x and H components of the FSV associated with the seasonal cycle \mathbf{S}_0 for $t_2 - t_1 = 365$ days and a 1 January start date for each coupled model. The FSVs for other start dates are very similar and not shown. Comparing Figs. 9a,b and 2a,c, Figs. 9c,d and 3a,c, and Figs. 9e,f and 5a,b shows that \mathbf{q}_1 and the FSV are qualitatively similar in all three models. A comparison of the FSVs for each hindcast trajectory described in section 3c reveals the same result: \mathbf{q}_1 and the FSV are always very similar.

Recall that the surface patterns of (u, v, T, S) for the 3D SVs at initial time (Moore et al. 2003) are also very similar to the patterns of $(\tau_x, \tau_y, H, E - P)$ of the SOs. Therefore it appears that irrespective of how a particular coupled model is perturbed, be it with an impulse, a forcing that is stochastic in time, or a forcing that is constant in time, the spatial pattern of the surface forcing that is optimal for producing the most rapid growth or largest variance in the Niño-3 index is the same in each case for time intervals ~ 12 months.

The Niño-3 index is an excellent indicator of the low-frequency variability of the tropical Pacific associated

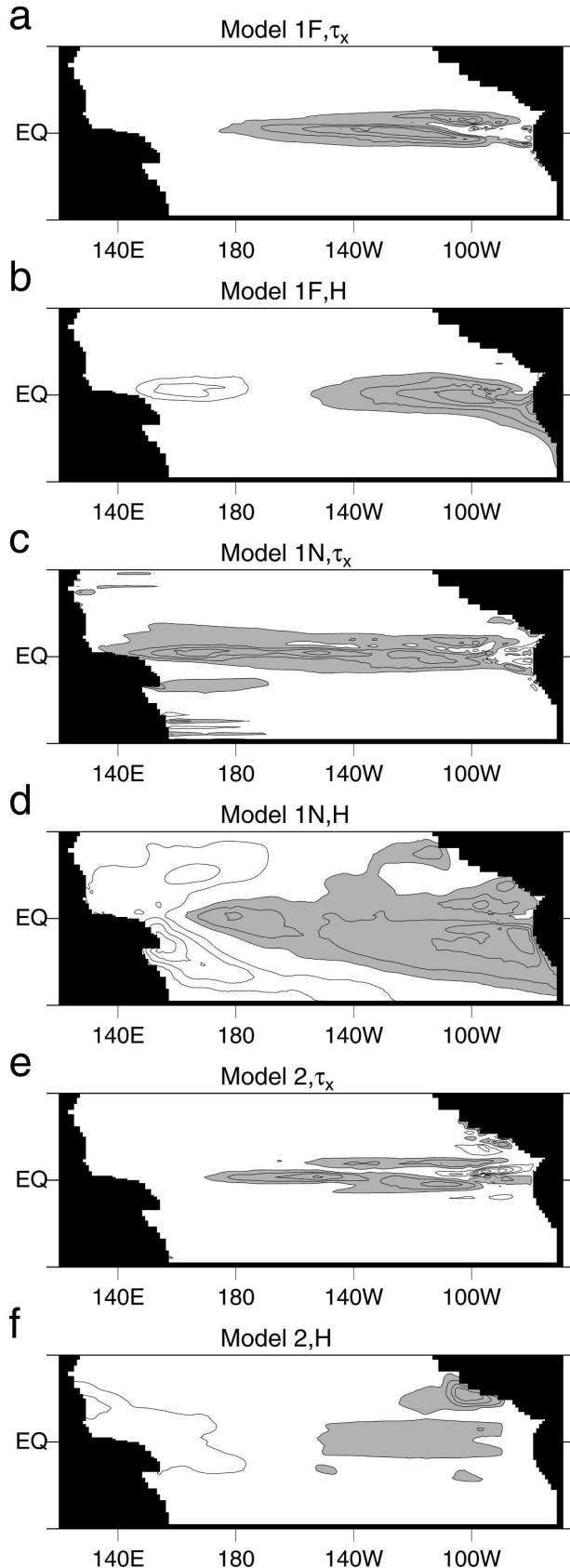


FIG. 9. The τ_x and H components of the FSVs of models (a), (b) 1F; (c), (d) 1N; and (e), (f) 2 for a 1 Jan start date using a seasonally varying basic state. In each case the contour interval is arbitrary, and shaded and unshaded regions are of opposite sign.

with ENSO. In each coupled model, ENSO is described by a single dominant coupled ocean–atmosphere mode (Moore et al. 2003). *On seasonal-to-interannual time scales, the only means of sustaining growth of the Niño-3-index is by exciting the ENSO mode. Since there is apparently only one dominant low-frequency ENSO mode in each coupled model, it is reasonable to assume that there is only one optimal excitation for this mode, irrespective of how the mode is forced.* If true in nature and more complex coupled GCMs, this result has important ramifications for data assimilation in support of seasonal forecasts, the growth of forecast errors, and ENSO predictability. This will be discussed in more detail in section 6.

5. Occurrence of the stochastic optimal patterns in atmospheric analyses

Sections 3 and 4 reveal that, for a given model, the geographic areas favored for perturbation growth by the SOs and FSVs are robust, but the areas favored do vary in time with the underlying \mathbf{S}_0 . Differences between the SOs and FSVs from model-to-model are substantial, and controlled by the atmospheric components as discussed in section 3d. Since each coupled model captures certain aspects of ENSO as observed (see Moore et al. 2003), it is natural to ask which of the SO patterns might be closest to that of ENSO in nature.

One possible way to answer this question is to see if perturbations like the SOs of the models ever appear in atmospheric analyses, which are our best estimate of nature. To do this we must first isolate the stochastic component $\mathbf{f}(t)$ of ocean surface forcing within the analyses. Unfortunately, there is no unique definition of $\mathbf{f}(t)$, and several can be found in the literature (e.g., Willebrand 1978; Frankignoul et al. 1979; Rienecker and Ehret 1988; Kleeman and Moore 1997). In the following, we draw on the analysis of Zavala-Garay et al. (2003) who define $\mathbf{f}(t)$ to be that component of surface forcing that is not instantaneously correlated with variations in SST. In this way $\mathbf{f}(t)$ represents the forcing due only to the internal variability of the atmosphere.

It is beyond the scope of the present paper to present the details of the Zavala-Garay et al. (2003) analysis. Suffice to say, their estimates of the stochastic forcing were derived from daily NCEP–NCAR reanalysis data of surface wind stress and heat flux.³ Because of the

TABLE 1. The mean and standard deviation (std dev) of 20-yr time series (1980–99) of the projection of \mathbf{q}_1 (namely, $\mathbf{f}_1^T \mathbf{f}_1 / \mathbf{f}^T \mathbf{f}$) on the stochastic component of the NCEP zonal wind stress for each model. Also shown is the 95% confidence interval (c.i.) based on the projection of $\mathbf{f}(t)$ on the two sets of 1000 randomly chosen fields described in section 5. One set of fields is spatially uncorrelated (c.i. random) and the other set is spatially correlated and computed from randomly chosen pairs of FSU wind anomalies (c.i. FSU).

Model	Mean	Std dev
Model 1F	0.22	0.12
Model 1N	0.24	0.13
Model 2	0.23	0.12
c.i. random	0.17	N/A
c.i. FSU	0.21	N/A

large uncertainties associated with the surface heat flux estimates, we restrict our attention to the zonal surface wind stress component of $\mathbf{f}(t)$.

We can represent $\mathbf{f}(t)$ as a linear combination of the SOs, so that $\mathbf{f}(t) = \sum_i a_i(t) \mathbf{q}_i$. Since the SOs form an orthonormal set (i.e., $\mathbf{q}_i^T \mathbf{q}_j = \delta_{ij}$) we can compute the amplitude a_i of any \mathbf{q}_i using the scalar-product $a_i(t) = \mathbf{q}_i^T \mathbf{f}(t)$. The contribution of any \mathbf{q}_i to \mathbf{f} is then given by $\mathbf{f}_i(t) = a_i(t) \mathbf{q}_i$. Table 1 shows the values of the time mean of $\mathbf{f}_1^T(t) \mathbf{f}_1(t) / \mathbf{f}^T(t) \mathbf{f}(t)$ and its standard deviation for the period 1980–99 computed using \mathbf{q}_1 from each model and for the annual mean basic state of section 3a. Table 1 indicates that, on average, \mathbf{q}_1 of models 1F, 1N, and 2 explains about 22%, 24%, and 23%, respectively, of the variance of \mathbf{f} , although at certain times this can be as large as 45% in all models based on variations of two standard deviations. These numbers are insensitive to whether the daily winds or time-averaged winds are used (we also explored weekly and monthly averages).

The statistical significance of the SO projections in Table 1 was estimated by comparing them with the projection of $\mathbf{f}(t)$ onto two randomly chosen sets of wind stress patterns: (i) spatially uncorrelated patterns created using a Gaussian random number generator, and (ii) spatially correlated patterns created by selecting at random pairs of monthly mean FSU wind stress anomaly fields for the tropical Pacific, then differencing the two fields. In each case 1000 orthogonal patterns were generated, denoted \mathbf{r}_i , $i = 1, \dots, 1000$, using a Gram–Schmidt orthogonalization procedure (Press et al. 1996). Each orthogonal pattern was normalized so that $\mathbf{r}_i^T \mathbf{r}_j = \delta_{ij}$, and the projection $b_i(t) = \mathbf{r}_i^T \mathbf{f}(t)$ computed. The relative contribution of each random pattern was then computed according to $p_i = \mathbf{w}_i^T(t) \mathbf{w}_i(t) / \mathbf{f}^T(t) \mathbf{f}(t)$, where $\mathbf{w}_i(t) = b_i(t) \mathbf{r}_i$. The time mean of the p_i will be denoted \bar{p}_i , and the mean of all 1000 \bar{p}_i will be denoted $\bar{\bar{p}}$ with standard deviation $\sigma_{\bar{\bar{p}}}$. In Table 1 the

³ Similar analyses of $\mathbf{f}(t)$ derived from daily ECMWF and monthly FSU winds are presented in Kleeman and Moore (1997) and Roulston and Neelin (2000), respectively.

values of $\bar{p} + 2\sigma_p$ computed using the two sets of random patterns are given and represent a measure of the 95% confidence interval (c.i.) that the variance explained by any SO is no more significant than that of a randomly chosen pattern of wind stress. Table 1 reveals that for each model the projection of \mathbf{q}_1 on \mathbf{f} is distinguishable from that of a randomly chosen field at the 95% confidence level, while the projections of \mathbf{q}_2 , \mathbf{q}_3 , and \mathbf{q}_4 are generally not significant (not shown). Table 1 therefore suggests that the dominant SOs of all three models are present in the real atmosphere if we accept that NCEP–NCAR reanalysis winds in the tropical Pacific provide reliable estimates of $\mathbf{f}(t)$ in nature.

6. Balanced truncation

The preceding analyses suggests that, on seasonal-to-interannual time scales, the effective dimension of the coupled ocean–atmosphere system (as distinct from either component alone) is small. In fact the existence of a single dominant coupled mode suggests that the system dimension may be $O(1)$. In this section we attempt to quantify this idea in a formal way using the method of balanced truncation (Moore 1981; Glover 1984; Farrell and Ioannou 2001a).

A method commonly used for attempting estimates of the dimensionality of an asymptotically stable dynamical system is to subject (1) to spatially uncorrelated, white noise forcing and then compute the eigenmodes of the covariance matrix $\mathbf{P} = \int_0^\infty \mathbf{X}^{1/2} \mathbf{R}(0, t) \mathbf{R}^T(t, 0) \mathbf{X}^{1/2} dt$ of the system response. The eigenmodes of \mathbf{P} are the EOFs of the system response, and each explains a specific fraction of the variance. Considering only those EOFs that account for a large fraction of the variance is therefore one way of attempting to identify the dominant degrees of freedom. However, Farrell and Ioannou (2001a) demonstrate that for nonnormal systems, using EOFs alone may be fundamentally misleading because they describe only a subset of the important system dynamics, and represent only the response of the system. Information about the perturbations that yield the EOF response may be lost because they may contribute little to the variance $\text{tr}[\mathbf{P}]$, and may be almost orthogonal to the EOFs. These perturbations are the eigenvectors of $\mathbf{Q} = \int_0^\infty \mathbf{R}^T(t, 0) \mathbf{X} \mathbf{R}(0, t) dt$, the SOs discussed earlier.

For nonnormal systems the appropriate method for state-space reduction is balanced truncation (Moore 1981; Glover 1984; Mehrmann and Stykel 2005), which seeks to simultaneously retain information contained in both the EOFs and SOs. In the present case, the dominant EOF describes the mature phase of the ENSO mode, while the dominant SO represents the optimal excitation of this mode, and both may have very differ-

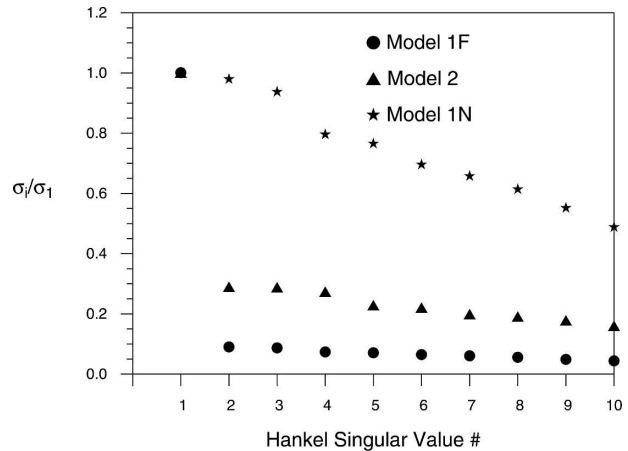


FIG. 10. A plot of σ_i/σ_1 for the first 10 members ($i = 1, \dots, 10$) of the Hankel singular value spectrum from each model using an annual mean basic state.

ent structures, as in model 2 (Moore and Kleeman 1999a, 2001).

The idea behind balanced truncation is to apply an internal coordinate transformation \mathbf{T} to \mathbf{s} described by (1) in which the EOFs and SOs become identical, and identify the dominant directions of variability in this new coordinate system in order to simultaneously identify relevant information described by both. The transformed variable $\mathbf{x} = \mathbf{T}\mathbf{s}$ and the transformed \mathbf{P} and \mathbf{Q} are given by $\tilde{\mathbf{P}} = \mathbf{T}\mathbf{P}\mathbf{T}^T$ and $\tilde{\mathbf{Q}} = \mathbf{T}^{-1}\mathbf{Q}\mathbf{T}^{-1}$ (Farrell and Ioannou 2001a). The coordinate transformation that simultaneously diagonalizes $\tilde{\mathbf{P}}$ and $\tilde{\mathbf{Q}}$ rendering them equal is given by $\mathbf{T} = \Sigma^{1/2} \mathbf{G}^T \mathbf{P}^{-1/2}$, where \mathbf{G} is the unitary matrix (i.e., $\mathbf{G}^T \mathbf{G} = \mathbf{I}$) that diagonalizes $\mathbf{P}^{1/2} \mathbf{Q} \mathbf{P}^{1/2}$ so that $\mathbf{P}^{1/2} \mathbf{Q} \mathbf{P}^{1/2} = \mathbf{G} \Sigma^2 \mathbf{G}^T$, and Σ is a diagonal matrix (Moore 1981; Glover 1984). The diagonal elements σ_i^2 of Σ^2 are the eigenvalues of $\mathbf{Q}\mathbf{P}$ arranged in descending order along the diagonal, and σ_i are called the Hankel singular values. In the new coordinate system the SOs and EOFs are identical, and the system is truncated by retaining only the first K Hankel singular values and corresponding SOs and EOFs.

Here we will consider the autonomous \mathbf{A} resulting from the annual mean basic state of section 3a.⁴ To capture variability outside the Niño-3 region, the norm used in this case was the basin-integrated squared SSTA. Figure 10 shows σ_i/σ_1 of each model for $i = 1, \dots, 10$, and reveals that σ_1 is an order of magnitude larger than the next member of the spectrum for model 1F, while for model 2, $\sigma_1 \sim 4\sigma_2$ and model 1N, $\sigma_1 \sim \sigma_2$. In all three models the ratio σ_1/σ_2 decreases (increases)

⁴ Practically, the upper limit of the integrals defining \mathbf{P} and \mathbf{Q} will be replaced by a finite time interval, which for the models used here is 365 days as discussed in section 3a.

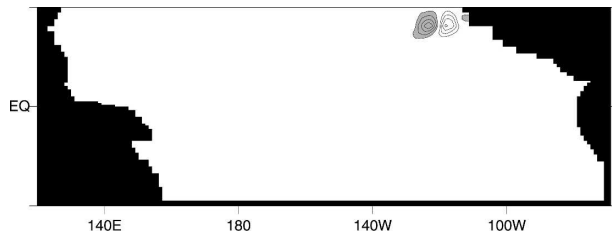


FIG. 11. The SST structure of the balanced truncation vector \mathbf{t}_2 showing how such structures are confined to regions of transient growth due to local shear in off-equatorial regions.

as the system moves away from the bifurcation point and becomes more (less) stable.

Computation of \mathbf{T} requires that we compute $\mathbf{P}^{-1/2}$, which is impractical. Instead, following M. Fisher et al. (2004, unpublished manuscript) a modified form of the Lanczos algorithm can be used to compute the eigenvectors of \mathbf{QP} given by $\hat{\mathbf{G}} = \mathbf{P}^{-1/2}\mathbf{G}$. Visual inspection reveals that the surface patterns of (u, v, T, S) for eigenvector $\mathbf{t}_1 = \sigma_1^{1/2}\mathbf{P}^{-1/2}\mathbf{g}_1$ for all models are almost identical to the patterns of $(\tau_x, \tau_y, H, E - P)$ for the 2D SOs shown in Figs. 2, 3, and 4. As noted in section 2, it is also possible to compute 3D SO patterns, and in this case \mathbf{t}_1 is qualitatively similar to the 3D SO of each model. The vectors $\mathbf{t}_2, \mathbf{t}_3$, etc. are associated with off-equatorial regions of localized barotropic and baroclinic transient growth that are not relevant to the low-frequency ENSO dynamics. To illustrate, Fig. 11 shows the SST structure of \mathbf{t}_2 that is common to all three models. Clearly only \mathbf{t}_1 is relevant to ENSO variability in the equatorial waveguide, a fact that highlights the apparent low dimensionality of the ENSO dynamics.

The dimension of a discrete dynamical operator is equal to the range of the operator, namely, the number of nonzero singular values. It is generally accepted that SVD is the most reliable method for determining numerically the rank of a matrix (Klema and Laub 1980; Golub and van Loan 1989). Balanced truncation is essentially a method for performing SVD on the dynamical operator that describes the time-integrated action of the system dynamics on stochastic forcing. It is important to note that the *entire* linearized discrete dynamical operator is used meaning that the balanced truncation vectors provide *direct* information about the rank and dimensionality of the discrete dynamical operator and its continuous counterpart. Therefore, in as much as the discretized model operators describe the true dynamics of the system, balanced truncation provides direct information about the dimensionality of the dynamics, and identifies the manifold on which the dynamics take place (Mehrmann and Stykel 2005).

Using models 1N and 2, Tang et al. (2005) have

shown that the predictability of ENSO is directly related to the amplitude of the ENSO eigenmode that is present in the forecast initial conditions. They have also demonstrated that data assimilation influences the predictive skill of ENSO forecasts via changes in the amplitude of the ENSO eigenmode in the initial conditions. The results of this section are in direct agreement with these ideas and show that the Tang et al. (2005) results may be explained by the dominant optimal excitation for the ENSO eigenmode. Any data assimilation or model initialization procedure that correctly maps onto this structure will increase the predictive skill of the ensuing forecast, an idea consistent with the recent work of Chang et al. (2004a,b) who showed that the EOFs associated with the dominant SOs are the most predictable components of the system.

7. Summary and conclusions

We have explored the optimal excitations of the low-frequency coupled ocean–atmosphere modes that approximate ENSO in three different coupled models, and considered the case where each model is subject to forcing that is either stochastic (SOs) or steady (FSVs) in time. We also compared these to the optimal forcing for an impulse function (SVs) calculated by Moore et al. (2003) for two of the same models.

Several features of the SO spectra and structures are noted: 1) Using an annual mean \mathbf{S}_0 , the SOs were found to be relatively insensitive to the time interval and decorrelation time assumed for the stochastic forcing; 2) using an annual mean \mathbf{S}_0 and temperature-based norms, the SO structures are relatively insensitive to the specific details of the chosen norm; 3) for annual mean and seasonally varying \mathbf{S}_0 , the SO spectrum is dominated by a single member; 4) for models with statistical atmospheres, the SOs are insensitive to the phase of the seasonal cycle or ENSO cycle; 5) for the model with a dynamical atmosphere and deep convection over the warm pool, SO heat flux patterns are sensitive to the phase of the seasonal cycle and ENSO cycle, although the same geographic areas are favored by the SOs for stochastically induced perturbation growth irrespective of \mathbf{S}_0 . However, the relative sensitivities of these different areas are seasonally dependent.

These findings are consistent with those reported by Kleeman and Moore (1997) and Moore and Kleeman (2001) using intermediate coupled models that utilized the same atmospheric components, and with SV analyses using two of the models considered here (Moore et al. 2003). The variations in SO and FSV structure between models can be explained in terms of the nonnor-

mality of the system eigenmodes in much the same way as discussed in Moore et al. (2003) in relation to the SVs.

Using the SOs of the annual mean basic state as representative of the optimal forcing patterns and optimal excitations for each model, we also explored whether similar structures are ever found in atmospheric analyses. This was done by computing the projection of the dominant SO patterns of each model onto estimates of the stochastic component of surface wind stress forcing derived from the NCEP–NCAR reanalyses. Patterns of variability resembling the dominant SO of each model are present, although the likelihood of finding the dominant SOs of each model appears to be the same.

It was found that irrespective of how a specific model is perturbed—namely, by an impulse, a steady forcing, or a forcing that is stochastic in time—the optimal forcing patterns or excitations for the low-frequency mode associated with ENSO are qualitatively similar to each other. This feature of the models was explored in terms of the effective dimension of each model using the method of balanced truncation. These calculations suggest that low-frequency variability of SST associated with ENSO is described by a low-dimensional system with $O(1)$ degrees of freedom. This is in qualitative agreement with analyses of observed time series of ENSO suggesting that the system has a low dimension (Bauer and Brown 1992; Ghil and Jiang 1998). Furthermore, the dominant balanced truncation eigenvector is remarkably similar to the dominant SO, suggesting that the predictability of ENSO may be associated with, or determined by, this single dominant pattern. Once this pattern has been identified, the potential exists for improving the efficiency of data assimilation in support of seasonal prediction (see Farrell and Ioannou 2001b), as well as improving the predictability of ENSO forecasts. The latter has been demonstrated by Tang et al. (2005) using a subset of the same coupled models used here, and their results are consistent with the idea of $O(1)$ degrees of freedom.

Acknowledgments. We are grateful to Brian Farrell for valuable discussions related to the material in section 6. This work was supported by a grant from the National Science Foundation (ATM 0112732). Any opinions, findings, and conclusions or recommendations expressed in this material are those of the authors and do not necessarily reflect the views of the National Science Foundation.

REFERENCES

- An, S.-I., and F. F. Jin, 2004: Nonlinearity and asymmetry of ENSO. *J. Climate*, **17**, 2399–2412.
- Anderson, D. L. T., 2004: Testing time for El Niño. *Nature*, **428**, 709–711.
- Balmaseda, M. A., M. K. Davey, and D. L. T. Anderson, 1995: Decadal and seasonal dependence of ENSO predictive skill. *J. Climate*, **8**, 2705–2715.
- Barkmeijer, J., T. Iversen, and T. N. Palmer, 2003: Forcing singular vectors and other sensitive model structure. *Quart. J. Roy. Meteor. Soc.*, **129**, 2401–2424.
- Barnett, T. P., M. Latif, N. Graham, M. Flügel, S. Pazan, and W. White, 1993: ENSO and ENSO related predictability. Part I: Prediction of equatorial sea surface temperature with a hybrid coupled ocean–atmosphere model. *J. Climate*, **6**, 1545–1566.
- Bauer, S. T., and M. G. Brown, 1992: Empirical low-order ENSO dynamics. *Geophys. Res. Lett.*, **19**, 2055–2058.
- Blanke, B., J. D. Neelin, and D. Gutzler, 1997: Estimating the effect of stochastic windstress forcing on ENSO irregularity. *J. Climate*, **10**, 1473–1486.
- Blumenthal, M. B., 1991: Predictability of a coupled ocean–atmosphere model. *J. Climate*, **4**, 766–784.
- Borges, M. D., and D. L. Hartmann, 1992: Barotropic instability and optimal perturbations of observed non-zonal flows. *J. Atmos. Sci.*, **49**, 335–354.
- Chang, P., R. Saravanan, T. DelSole, and F. Wang, 2004a: Predictability of linear coupled systems. Part I: Theoretical analyses. *J. Climate*, **17**, 1474–1486.
- , —, F. Wang, and L. Ji, 2004b: Predictability of linear coupled systems. Part II: An application to a simple model of tropical Atlantic variability. *J. Climate*, **17**, 1487–1503.
- Chen, D., M. A. Cane, A. Kaplan, S. E. Zebiak, and D. Huang, 2004: Predictability of El Niño over the past 148 years. *Nature*, **428**, 733–736.
- Chhak, K. C., A. M. Moore, R. F. Milliff, G. Branstator, W. R. Holland, and M. Fisher, 2006: Stochastic forcing of the North Atlantic wind-driven ocean circulation. Part I: A diagnostic analysis of the ocean response to stochastic forcing. *J. Phys. Oceanogr.*, **36**, 300–315.
- Eckert, C., and M. Latif, 1997: Predictability of a stochastically forced hybrid coupled model of El Niño. *J. Climate*, **10**, 1488–1504.
- Eisenman, I., L. Yu, and E. Tziperman, 2005: Westerly wind bursts: ENSO’s tail rather than the dog? *J. Climate*, **18**, 5224–5238.
- Fan, Y., M. R. Allen, D. L. T. Anderson, and M. A. Balmaseda, 2000: How predictability depends on the nature of uncertainty in initial conditions in a coupled model of ENSO. *J. Climate*, **13**, 3298–3313.
- Farrell, B. F., and P. J. Ioannou, 1993: Stochastic forcing of the linearized Navier–Stokes equations. *Phys. Fluids A*, **5**, 2600–2609.
- , and —, 1996a: Generalized stability theory. Part I: Autonomous operators. *J. Atmos. Sci.*, **53**, 2025–2040.
- , and —, 1996b: Generalized stability theory. Part II: Non-autonomous operators. *J. Atmos. Sci.*, **53**, 2041–2053.
- , and —, 2001a: Accurate low-dimensional approximation of the linear dynamics of fluid flow. *J. Atmos. Sci.*, **58**, 2771–2789.
- , and —, 2001b: State estimation using a reduced-order Kalman filter. *J. Atmos. Sci.*, **58**, 3666–3680.
- Federov, A. V., S. L. Harper, S. G. Philander, B. Winter, and A. Wittenberg, 2003: How predictable is El Niño? *Bull. Amer. Meteor. Soc.*, **84**, 911–919.
- Frankignoul, C., P. Müller, and E. Zorita, 1997: A simple model of

- the decadal response of the ocean to stochastic wind forcing. *J. Phys. Oceanogr.*, **27**, 1533–1546.
- Frederiksen, J. S., 1982: A unified three-dimensional instability theory of the onset of blocking and cyclogenesis. *J. Atmos. Sci.*, **39**, 969–982.
- Ghil, M., and N. Jiang, 1998: Recent forecast skill for the El Niño/Southern Oscillation. *Geophys. Res. Lett.*, **25**, 171–174.
- Giering, R., and T. Kaminski, 1998: Recipes for adjoint code construction. *ACM Trans. Math. Software*, **24**, 437–474.
- Gill, A. E., 1980: Simple solutions for heat-induced tropical circulation. *Quart. J. Roy. Meteor. Soc.*, **106**, 447–462.
- Glover, K., 1984: An optimal Hankel-norm approximation of linear multivariate systems and their L^∞ -error bounds. *Int. J. Control*, **39**, 1115–1193.
- Golub, G. H., and C. F. van Loan, 1989: *Matrix Computations*. Johns Hopkins University Press, 642 pp.
- Horsthemke, W., and R. Lefever, 1984: *Noise-Induced Transitions: Theory and Applications in Physics, Chemistry and Biology*. Springer-Verlag, 318 pp.
- Johnson, S., 1999: Markov model studies of the El Niño Southern Oscillation. Ph.D. thesis, University of Washington, 143 pp.
- Kalnay, E., and Coauthors, 1996: NCEP/NCAR 40-Year Reanalysis Project. *Bull. Amer. Meteor. Soc.*, **77**, 437–471.
- Keen, R. A., 1987: Equatorial westerlies and the Southern Oscillation. *USTOGA 8: Proc. U.S. TOGA Western Pacific Air-Sea Interaction Workshop*, Boulder, CO, UCAR, 121–140.
- Kessler, W. S., 2001: EOF representations of the Madden-Julian oscillation and its connection with ENSO. *J. Climate*, **14**, 3055–3061.
- Kleeman, R., 1991: A simple model of the atmospheric response to ENSO sea surface temperature anomalies. *J. Atmos. Sci.*, **48**, 3–18.
- , and A. M. Moore, 1997: A theory for the limitations of ENSO predictability due to stochastic atmospheric transients. *J. Atmos. Sci.*, **54**, 753–767.
- , J. P. McCreary, and B. A. Klinger, 1999: A mechanism for generating ENSO decadal variability. *Geophys. Res. Lett.*, **26**, 1743–1746.
- , Y. Tang, and A. M. Moore, 2003: The calculation of climatically relevant singular vectors in the presence of weather noise. *J. Atmos. Sci.*, **60**, 2856–2868.
- Klema, V. C., and A. J. Laub, 1980: The singular value decomposition: Its computation and some applications. *IEEE Trans. Automatic Control*, **AC-25**, 164–176.
- Latif, M., and A. Villwock, 1990: Interannual variability in the tropical Pacific as simulated in coupled ocean-atmosphere models. *J. Mar. Syst.*, **1**, 51–60.
- , and M. Flügel, 1991: An investigation of short range climate predictability in the tropical Pacific. *J. Geophys. Res.*, **96**, 2661–2673.
- Lau, K.-M., 1985: Elements of a stochastic dynamical theory of the long-term variability of the El Niño/Southern Oscillation. *J. Atmos. Sci.*, **42**, 1552–1558.
- , and P. H. Chan, 1985: Aspects of the 40–50 day oscillation during the northern winter as inferred from outgoing long-wave radiation. *Mon. Wea. Rev.*, **113**, 1889–1909.
- , and —, 1986: The 40–50 day oscillation and the El Niño/Southern Oscillation: A new perspective. *Bull. Amer. Meteor. Soc.*, **67**, 533–534.
- , and —, 1988: Intraseasonal and interannual variations of tropical convection: A possible link between 40–50 day oscillation and ENSO? *J. Atmos. Sci.*, **45**, 506–521.
- Legler, D. M., and J. J. O'Brien, 1985: *Atlas of Tropical Pacific Wind-Stress Climatology, 1971–1980*. The Florida State University, 187 pp.
- Lehoucq, R. B., D. C. Sorensen, and C. Yang, 1998: *ARPACK Users Guide: Solution of Large Scale Eigenvalue Problems with Implicitly Restarted Arnoldi Methods*. SIAM, 142 pp.
- Lengaigne, M., E. Guilyardi, J.-P. Boulanger, C. Menkes, P. Delecluse, P. Inness, J. Cole, and J. Slingo, 2004: Triggering of El Niño by westerly wind bursts in a coupled general circulation model. *Climate Dyn.*, **23**, 601–620.
- Levitus, S., 1982: *Climatological Atlas of the World Ocean*. NOAA Prof. Paper 13, 173 pp. and 17 microfiche.
- Madec, G., P. Delecluse, M. Imbard, and C. Levy, 1998: OPA 8.1 ocean general circulation model reference manual. Institut Pierre-Simon Laplace des Sciences l'Environnement Global, LODYC, Université Pierre et Marie Curie, Paris, France, 97 pp.
- McPhaden, M. J., 1999: Genesis and evolution of the 1997–98 El Niño. *Science*, **283**, 950–954.
- Mehrmann, V., and T. Stykel, 2005: Balanced truncation model reduction for large scale systems in descriptor form. *Dimension Reduction of Large-Scale Systems*. P. Benner, V. Mehrmann, and D. C. Sorensen, Eds., Lecture Notes in Computational Science and Engineering, Vol. 45, Springer-Verlag, 83–115.
- Molteni, F., and T. N. Palmer, 1993: Predictability and finite-time instability of the northern winter circulation. *Quart. J. Roy. Meteor. Soc.*, **119**, 269–298.
- Moore, A. M., and R. Kleeman, 1996: The dynamics of error growth and predictability in a coupled model of ENSO. *Quart. J. Roy. Meteor. Soc.*, **122**, 1405–1446.
- , and —, 1997a: The singular vectors of a coupled ocean-atmosphere model of ENSO. Part I: Thermodynamics, energetics and error growth. *Quart. J. Roy. Meteor. Soc.*, **123**, 953–981.
- , and —, 1997b: The singular vectors of a coupled ocean-atmosphere model of ENSO. Part II: Sensitivity studies and dynamical significance. *Quart. J. Roy. Meteor. Soc.*, **123**, 983–1006.
- , and —, 1999a: Stochastic forcing of ENSO by the intraseasonal oscillation. *J. Climate*, **12**, 1199–1220.
- , and —, 1999b: The nonnormal nature of El Niño and intraseasonal variability. *J. Climate*, **12**, 2965–2982.
- , and —, 2001: The differences between the optimal perturbations of coupled models of ENSO. *J. Climate*, **14**, 138–163.
- , J. Vialard, A. T. Weaver, D. L. T. Anderson, R. Kleeman, and J. R. Johnson, 2003: The role of air-sea interaction in controlling the optimal perturbations of low-frequency tropical coupled ocean-atmosphere modes. *J. Climate*, **16**, 951–968.
- Moore, B. C., 1981: Principal component analysis in linear systems: Controllability, observability, and model reduction. *IEEE Trans. Automatic Control*, **AC-26**, 17–31.
- Pedlosky, J., 1987: *Geophysical Fluid Dynamics*. Springer-Verlag, 710 pp.
- Penland, C., 1996: A stochastic model of Indo-Pacific sea surface temperature anomalies. *Physica D*, **98**, 534–558.
- , and P. D. Sardeshmukh, 1995: The optimal growth of tropical sea surface temperature anomalies. *J. Climate*, **8**, 1999–2024.
- Perez, C. L., A. M. Moore, J. Zavala-Garay, and R. Kleeman, 2005: A comparison of the influence of additive and multi-

- plicative stochastic forcing on a coupled model of ENSO. *J. Climate*, **18**, 5066–5085.
- Press, W. H., S. A. Teukolsky, W. T. Vetterling, and B. P. Flannery, 1996: *Numerical Recipes in Fortran 77: The Art of Scientific Computing*. Vol 1. 2d ed. Cambridge University Press, 933 pp.
- Reynolds, R. W., and T. M. Smith, 1994: Improved global sea surface temperature analyses using optimum interpolation. *J. Climate*, **7**, 929–948.
- Rienecker, M. M., and L. L. Ehret, 1988: Wind stress curl variability over the North Pacific from the Comprehensive Ocean–Atmosphere Data Set. *J. Geophys. Res.*, **93**, 5069–5077.
- Roulston, M. S., and J. D. Neelin, 2000: The response of an ENSO model to climate noise, weather noise and intraseasonal forcing. *Geophys. Res. Lett.*, **27**, 3723–3726.
- , and —, 2003: Non-linear coupling between modes in a low-dimensional model of ENSO. *Atmos.–Ocean*, **41**, 217–231.
- Simmons, A. J., and B. J. Hoskins, 1976: Baroclinic instability on the sphere: Normal modes of the primitive and quasigeostrophic equations. *J. Atmos. Sci.*, **33**, 1454–1477.
- , J. M. Wallace, and G. W. Branstator, 1983: Barotropic wave propagation, and instability and atmospheric teleconnection patterns. *J. Atmos. Sci.*, **40**, 1363–1392.
- Stricherz, J., J. J. O'Brien, and D. M. Legler, 1992: Florida State University tropical Pacific winds for TOGA 1966–1985. The Florida State University, 250 pp.
- , D. M. Legler, and J. J. O'Brien, 1997: *Pacific Ocean*. Vol. II, *TOGA Pseudo-Stress Atlas 1985–1994*, The Florida State University, 155 pp.
- Syu, H.-H., J. D. Neelin, and D. S. Gutzler, 1995: Seasonal and interannual variability in a hybrid coupled GCM. *J. Climate*, **9**, 2121–2143.
- Tang, Y., R. Kleeman, A. M. Moore, A. T. Weaver, and J. Vialard, 2003: The use of ocean reanalysis products to initialize ENSO predictions. *Geophys. Res. Lett.*, **30**, 1694, doi:10.1029/2003GL017664.
- , —, and —, 2004a: SST assimilation experiments in a tropical Pacific Ocean model. *J. Phys. Oceanogr.*, **34**, 623–642.
- , —, —, J. Vialard, and A. T. Weaver, 2004b: An off-line, numerically efficient initialization scheme in an oceanic general circulation model for El Niño Southern Oscillation prediction. *J. Geophys. Res.*, **109**, C0514, doi:10.1029/2003JC002159.
- , —, and —, 2005: On the reliability of ENSO dynamical predictions. *J. Atmos. Sci.*, **62**, 1770–1791.
- Thompson, C. J., 1998: Initial conditions for optimal growth in a coupled ocean–atmosphere model of ENSO. *J. Atmos. Sci.*, **55**, 537–557.
- Tziperman, E., L. Stone, M. A. Cane, and H. Jarosh, 1994: El Niño chaos: Overlapping of resonances between the seasonal cycle and the Pacific ocean–atmosphere oscillator. *Science*, **264**, 72–74.
- , M. A. Cane, and S. E. Zebiak, 1995: Irregularity and locking to the seasonal cycle in an ENSO prediction model as explained by the quasi-periodicity route to chaos. *J. Atmos. Sci.*, **52**, 293–306.
- Vialard, J., and P. Delecluse, 1998a: An OGCM study for the TOGA decade. Part I: Role of salinity in the physics of the western Pacific fresh pool. *J. Phys. Oceanogr.*, **28**, 1071–1088.
- , and —, 1998b: An OGCM study for the TOGA decade. Part II: Barrier layer formation and variability. *J. Phys. Oceanogr.*, **28**, 1089–1106.
- , C. Menkes, J.-P. Boulanger, P. Delecluse, E. Guilyardi, and M. J. McPhaden, 2001: A model study of oceanic mechanisms affecting equatorial Pacific sea surface temperature during the 1997–98 El Niño. *J. Phys. Oceanogr.*, **31**, 1649–1675.
- , —, D. L. T. Anderson, and M. Balmaseda, 2003: Sensitivity of Pacific Ocean tropical instability waves to initial conditions. *J. Phys. Oceanogr.*, **33**, 105–121.
- Weaver, A. T., J. Vialard, and D. L. T. Anderson, 2003: Three- and four-dimensional variational assimilation with a general circulation model of the tropical Pacific Ocean. Part I: Formulation, internal diagnostics, and consistency checks. *Mon. Wea. Rev.*, **131**, 1360–1378.
- Webster, P. J., 1972: Response of the tropical atmosphere to local steady forcing. *Mon. Wea. Rev.*, **100**, 518–541.
- Willebrand, J., 1978: Temporal and spatial scales of the wind field over the North Pacific and North Atlantic. *J. Phys. Oceanogr.*, **8**, 1080–1094.
- Xue, Y., M. A. Cane, S. E. Zebiak, and M. B. Blumenthal, 1994: On the prediction of ENSO: A study with a low order Markov model. *Tellus*, **46A**, 512–528.
- , —, and —, 1997a: Predictability of a coupled model of ENSO using singular vector analysis. Part I: Optimal growth in seasonal background and ENSO cycles. *Mon. Wea. Rev.*, **125**, 2043–2056.
- , —, and —, 1997b: Predictability of a coupled model of ENSO using singular vector analysis. Part II: Optimal growth and forecast skill. *Mon. Wea. Rev.*, **125**, 2057–2073.
- Zavala-Garay, J., A. M. Moore, C. L. Perez, and R. Kleeman, 2003: The response of a coupled model of ENSO to observed estimates of stochastic forcing. *J. Climate*, **16**, 2827–2842.